



# Ferrimagnetism state in $\text{FeMn}_2\text{O}_{4-\delta}$ epitaxial films on MgO(100) substrate

Duong Van Thiet<sup>1,\*</sup> , Nguyen Xuan Chung<sup>2</sup>, Nguyen Quoc Tuan<sup>1</sup>, Nguyen Tien Tung<sup>1</sup>, Ha Thanh Hai<sup>1</sup>, Do Ngoc Tu<sup>1</sup>, and Sunglae Cho<sup>3</sup>

<sup>1</sup> School of Mechanical and Automotive Engineering, Hanoi University of Industry, Hanoi 100000, Vietnam

<sup>2</sup> Department of Physics, Hanoi University of Mining and Geology, Pho Vien 18, Duc Thang, Bac Tu Liem, Hanoi 100000, Vietnam

<sup>3</sup> Department of Physics and Energy Harvest Storage Research Center, University of Ulsan, Ulsan 680-749, Republic of Korea

**Received:** 30 August 2024

**Accepted:** 24 December 2024

© The Author(s), under exclusive licence to Springer Science+Business Media, LLC, part of Springer Nature, 2025

## ABSTRACT

$\text{FeMn}_2\text{O}_{4-\delta}$  epitaxial films were grown on a MgO (100) substrate by using molecular beam epitaxy (MBE) at low growth temperature from 100 to 300 °C in oxygen-cracked environment. The results shows that the structural properties of films are single crystalline with flat surface at growth temperatures of 200 °C. The tensile strain of films decrease as growth temperature increase which is confirmed by X-ray diffraction characterization. The optical band gaps of films are 3.44, 3.50, and 3.20 eV with growth temperatures of 100 °C, 200 °C, and 300 °C, respectively. In addition, the films possess magnetic properties in ferrimagnetic ordering at room temperature without any magnetic transition below this temperature; magnetization of films decreases as growth temperature increase. The results average magnetic moment per unit are estimated to be 3.72, 2.84, and 2.13  $\mu_B/\text{f.u}$  corresponding to 100 °C, 200 °C, and 300 °C of growth temperature. Our work provides a study on structural and magnetic properties of  $\text{FeMn}_2\text{O}_{4-\delta}$  in thin film form, which has potential application in fabrication of spin-filter devices.

## 1 Introduction

Spinel oxide is usually represented by  $(A_{1-\delta}B_\delta)[B_{2-\delta}A_\delta]O_4$ ,  $\delta$  is the inversion parameter, compound in the round stands for the cations occupying on tetrahedral (T), while the one in square brackets represents octahedral (O) sites. The case of  $x = 0$  is called normal spinel,  $x = 1$  is full inverse spinel and  $0 < x < 1$  is mixed spinel [1]. The spinel oxide thin film has potential applications in magnetic detector, magnetic memory – spintronics devices, such as magnetic random access memories and spin metal oxide semiconductor field

effect transistors. Besides, this material can be used for electrodes in energy storage devices (supercapacitor, lithium batteries, catalysts, photoelectrodes). One of most popular materials for above applications is spinel ferrite and spinel manganite [2]. Spin-filter are devices that operating based on tunneling magnetoresistance (TMR) effect and are key spintronic component both for sensing and generating spin-polarized current. Its main structure consists of two layers are ferromagnetic and non-magnetic material contact together. To generate huge spin-polarized electron current in spin-filter devices, the ferromagnetic materials need

Address correspondence to E-mail: dvthiet86@haui.edu.vn

to possess properties such as half-metal, high resistivity, high Curie temperature, high crystal quality and large saturation magnetization [3]. However, currently there are only few oxides that satisfy the above issues: for instance EuO ( $T_C = 69$  K) [4], perovskite oxides BiMnO<sub>3</sub> ( $T_C = 105$  K) [5], spinel oxides based on Fe<sub>3</sub>O<sub>4</sub> ( $T_C = 858$  K), NiFe<sub>2</sub>O<sub>4</sub> ( $T_C = 850$  K), CoFe<sub>2</sub>O<sub>4</sub> ( $T_C = 793$  K), and MnFe<sub>2</sub>O<sub>4</sub> ( $T_C = 573$  K) [3]. So it is crucial to find out similar materials to above ones.

FeMn<sub>2</sub>O<sub>4</sub> has been an attractive material because of its excellent magnetic characteristics and energy storage field [6–15]. According to theoretical calculation, FeMn<sub>2</sub>O<sub>4</sub> is faced-centered-cubic and the space group Fd  $\bar{3}$  m and predicted as one half-metallic which is considered as a promising material for spin filters [9]. In bulk form single crystal, FeMn<sub>2</sub>O<sub>4</sub> has tetragonal crystal structure (I41/amd) with  $a = b = 5.91$  Å and  $c = 8.91$  Å, it undergoes one structure-transition temperature of 595 K, from cubic to tetragonal as temperature reduces; and two ferrimagnetic transitions occur at 373 K and 50 K [10]. In other experiments, the structure of FeMn<sub>2</sub>O<sub>4</sub> is mixed spinel oxide with the presence of Fe<sup>3+</sup> and Mn<sup>2+</sup> ions at tetrahedral site [11–15]. However, there have not been reports about properties of FeMn<sub>2</sub>O<sub>4</sub> thin films yet. So in this work, structural, and magnetic properties of FeMn<sub>2</sub>O<sub>4-6</sub> thin films at different growth temperatures by using molecular beam epitaxy (MBE) are represented. The films showed single crystal in all samples while the best crystal and flat surface at a growth temperature of 200 °C. They are not conductive at room temperature with band gaps of 3.44, 3.50, and 3.20 eV for growth temperature of 100 °C, 200 °C, and 300 °C, respectively. They also show ferrimagnetism state with magnetization decreases for higher growth temperature. These results possibly confirm that FeMn<sub>2</sub>O<sub>4-6</sub> thin film can be used as a magnetic tunnel barrier in spin-filter devices in spintronics field.

## 2 Experiment

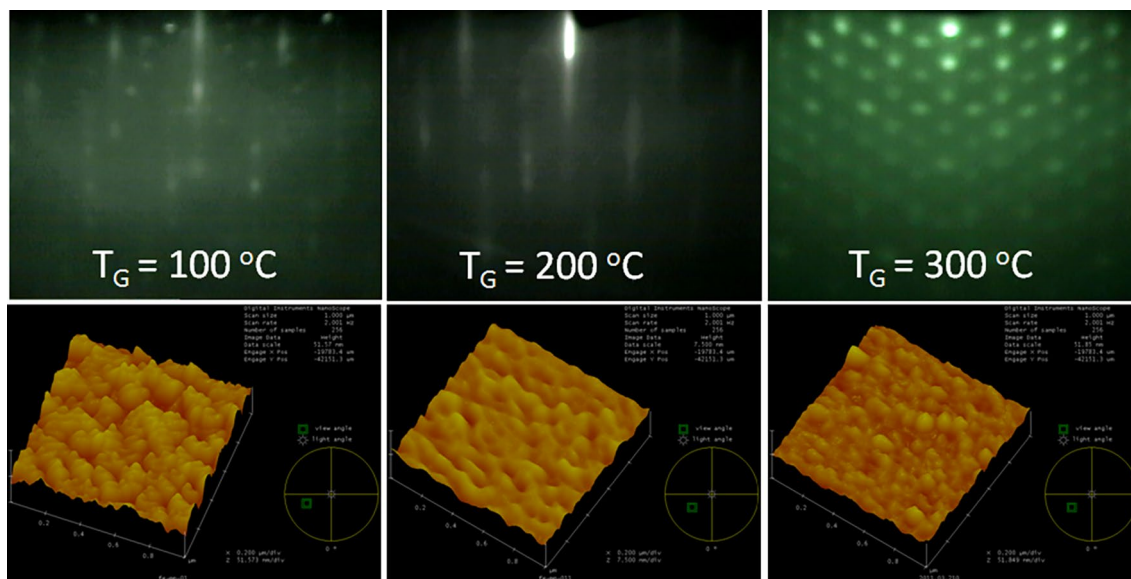
The FeMn<sub>2</sub>O<sub>4-6</sub> films were grown on a MgO(100) substrate by MBE system (VG Semicon. Inc.), with a low base pressure of chamber (around 10<sup>-9</sup> Torr) under the growth temperatures of 100 °C, 200 °C, and 300 °C. To form FeMn<sub>2</sub>O<sub>4-6</sub> atomic oxygen gas were filled by using an oxygen cracking cell. Evaporation of Mn, Fe was conducted by using effusion cells under pressure of 10<sup>-6</sup> Torr of oxygen gas. As grown, the film quality

was monitored by *in-situ* reflection high-energy electron diffraction (RHEED), while the film's topography was inspected by *ex-situ* atomic force microscopy (AFM) (SIINanoTechnology Inc., K—A102006344) in a tapping mode. X-ray diffraction (XRD) was used to investigate the phase and growth orientation of the films, the range ( $2\theta$ ) of scanning was set between 20° and 120°. Raman spectroscopy was conducted at room temperature, in the range between 200 and 800 cm<sup>-1</sup> using an Ar + laser 532 nm beam with a power of 5 mW, and beam diameter of 50 μm. X-ray photoelectron spectroscopy (XPS) was used to investigate the valence states of Mn, Fe, and O. The optical band gap was investigated by spectroscopy of ellipsometry. The magnetic properties were observed on a superconducting quantum interference device (SQUID) magnetometer (Quantum Design, Inc.).

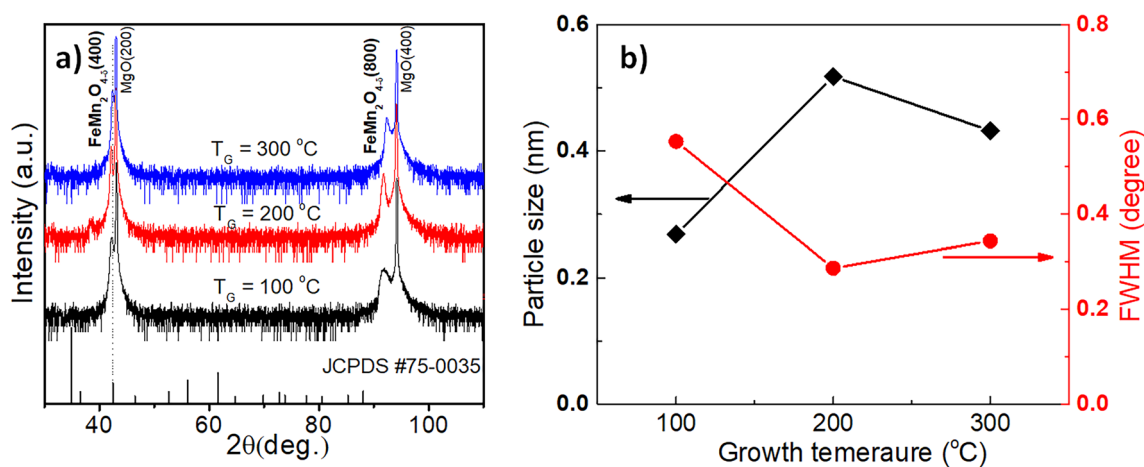
## 3 Result and discussion

Figure 1a–c shows RHEED pattern of FeMn<sub>2</sub>O<sub>4-6</sub> films after finishing growth. The RHEED patterns are Kikuchi lines combining spotty pattern of growth temperature of 100 °C in Fig. 1a. While Kikuchi lines patterns and spotty patterns appear at 200 and 300 °C, respectively. The results indicate that the film's surface under growth temperature of 200 °C are flat with the best crystalline. The results are confirmed more by using AFM investigation in 1 × 1 μm<sup>2</sup> scale. The root-mean square roughnesses (RMS) are 5.824, 0.562, and 3.448 nm at growth temperatures of 100, 200, and 300 °C, respectively.

The results of XRD patterns of films are shown in Fig. 2a. There are two peaks (400) and (800) which are assigned to bulk FeMn<sub>2</sub>O<sub>4</sub> in card JCPDS: PDF #75–0035 and similar orientation with the MgO substrate; no other peak is observed within XRD technique, indicating these single crystalline films. The lattice constant of bulk FeMn<sub>2</sub>O<sub>4</sub> is 8.510 Å while the one of MgO ( $2a_{\text{bulk}}$ ) is found at 8.438 Å, this result suggests that FeMn<sub>2</sub>O<sub>4-6</sub> grows in-plane compression strain of 0.85%. As can be seen that the (400) diffraction peak of FeMn<sub>2</sub>O<sub>4-6</sub> films shift to larger angle for high growth temperature, indicating a decrease in the out-of-plane  $d$  spacing. These determined values of 2.1449, 2.1426, and 2.1323 Å correspond to annealing temperatures of 100 °C, 200 °C, and 300 °C, respectively. Comparison to the value of bulk (2.1275 Å, FeMn<sub>2</sub>O<sub>4</sub>-JCPDS: PDF #75-0035), it indicates that tensile strains



**Fig. 1** (Color online): **a–c** RHEED patterns and **d–f** AFM images of  $\text{FeMn}_2\text{O}_{4.6}$  films at growth temperatures 100 °C, 200 °C and 300 °C, respectively



**Fig. 2** (Color online): **a** XRD patterns  $\text{FeMn}_2\text{O}_{4.6}$  films on  $\text{MgO}(100)$  substrate at growth temperatures 100 °C, 200 °C and 300 °C, **b** Full width at half maximum (FWHM) and particle size of (400) peak peak (400) of  $\text{FeMn}_2\text{O}_{4.6}$  films

of films are perpendicular to their surfaces. The value of the tensile strain reducing as growth temperature increases can be explained by the 0.85% mismatch between  $\text{MgO}$  substrate and the  $\text{FeMn}_2\text{O}_4$  epilayer. The compression strain gives a rise to a lateral shrink in-plane, which leads to an increase in the interatomic separations normal to the surface. The Full width at half maximum (FWHM) and particle size of (400) peak as a function of the growth temperature is shown in Fig. 2b. The growth temperature of 200 °C shows the smaller FWHM and larger particle size values,

indicating the higher crystalline, consistent with the RHEED pattern.

The Raman spectrum of  $\text{FeMn}_2\text{O}_{4.6}$  films were measured at room temperature to inspect depth regarding to local structure. However, up to now, there has been no report about Raman spectrum of  $\text{FeMn}_2\text{O}_4$ . Laser beam of 532 nm was used, the frequency range detection was set between 200 and 800  $\text{cm}^{-1}$ . In cubic spinel structural, there are five Raman active modes:  $A_{1g}$ ,  $E_g$  and  $3T_{2g}$  [16]. There are four Raman modes of  $\text{FeMn}_2\text{O}_{4.6}$  films at 314, 459, 621, and 675  $\text{cm}^{-1}$  which

correspond to the  $E_g$ ,  $T_{2g}$  (2) and  $A_{1g}$  mode, respectively, while the two peaks at 621 and 675  $\text{cm}^{-1}$  are considered as the split of mode  $A_{1g}$  as shown in Fig. 3. In cubic spinel oxides, the splitting, shouldering or broadening of  $A_{1g}$  mode present disorder effect of cation  $M^{2+}$  and  $Fe^{3+}$  over the tetragonal and octahedral sites, meanwhile the modes above 600  $\text{cm}^{-1}$  usually correspond to the motion of oxygen atom in the tetrahedral  $AO_4$  group [17–25]. It is known that  $Fe_3O_4$  has a fully inverse spinel structure. The  $A_{1g}$  Raman mode is found as asymmetric peak due to only  $Fe^{3+}$  cation fully occupying at tetragonal sites [21]. Nevertheless, in the case of  $FeMn_2O_{4-6}$  at tetrahedral sites appear both  $Mn^{2+}$

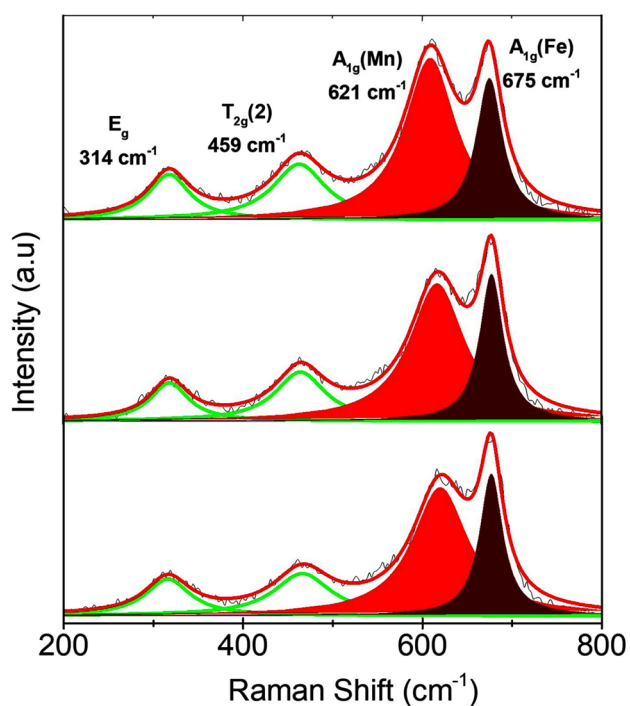


**Fig. 3** (Color online) Raman spectrum active vibration modes of  $FeMn_2O_{4-6}$  films at growth temperatures 100 °C, 200 °C and 300 °C

and  $Fe^{3+}$  cations [10, 11], which is caused by splitting into two Raman modes  $A_{1g}(Mn^{2+}-O) < A_{1g}(Fe^{3+}-O)$ . Because ionic radius of  $Mn^{2+}$  (0.80 Å) is larger than that of  $Fe^{3+}$  (0.64 Å) [26], the variation of bond length derives from the replacement of cations  $Mn^{2+}$  on  $Fe^{3+}$  at tetrahedral sites, two Raman modes  $A_{1g}$  appear. This result agrees with some previous publications on spinel oxides such as  $MgFe_2O_4$  [18],  $NiFe_2O_4$  [19], and  $CoFe_2O_4$  [20]]. These spinel structures are found to be fully inverse spinel and partly inverse spinel. The difference about Raman active mode value between  $FeMn_2O_{4-6}$  films and other spinel oxide are indicated as Table 1 below. By using qualitatively fit at tetrahedral sites, the red and brown area exhibit distribution of  $Mn^{2+}$  and  $Fe^{3+}$  cations, respectively the variation of  $Fe^{3+}/Mn^{2+}$  ratio at different growth temperature is almost similar.

The valance states of cations on film's surface are investigated by XPS spectra as shown in Fig. 4a–c corresponding to Fe 2p, Mn 2p, and O 1s. Figure 4a presents the Fe 2p spectra, with two main peaks of  $Fe2p_{3/2}$  and  $Fe2p_{1/2}$  split spin–orbit component of 13.9 eV. By applying Gaussing distribution function, the peaks position at 710.6 eV and 724.5 eV confirms oxidation states of  $Fe^{2+}$  while peaks at 712.5 eV and 726.3 eV assign to oxidation states of  $Fe^{3+}$ . The Fe 2p spectra of  $FeMn_2O_{4-6}$  films have characterization like to Fe 2p spectra of  $\gamma\text{-}Fe_2O_3$ , which has spinel structure constituted by  $Fe^{3+}$  in octahedral and tetrahedral sites [27]. In Fig. 4b illustrates exhibited Mn 2p spectra with two main peaks of  $Mn 2p_{3/2}$  and  $Mn 2p_{1/2}$ ; split spin–orbit components of 11.6 eV. The peaks at 641.5 eV and 653.2 eV correspond to  $Mn^{2+}$  valance, while the peaks at 642.5 and 654.2 eV present  $Mn^{3+}$  valance. Figure 4c presents O 1s spectra with two peaks while the peak at 530.5 eV exhibits metal–oxygen bonds (O1s-a); the peak at 531.3 eV is allocated to defect sites and chemisorbed water at surface of films. As can be seen from analyzing XPS spectra,

**Table 1** Raman data of some  $AB_2O_4$  spinel oxide. Shoulders of peaks are marked with “sh”

Spinel oxide	Mode ( $\text{cm}^{-1}$ )				
	$T_{2g}(1)$	$E_g$	$T_{2g}(2)$	$T_{2g}(3)$	$A_{1g}$
$FeMn_2O_{4-6}$ [Our work]		314	459		621, 675
$MgFe_2O_4$ [18]	217	333	486	554	646, 715
$NiFe_2O_4$ [19]	211	335	450sh, 487	567sh, 596	659sh, 703
$CoFe_2O_4$ [20]	207	305	470	580	615sh, 693
$Fe_3O_4$ [21]	205	310	380	538	665

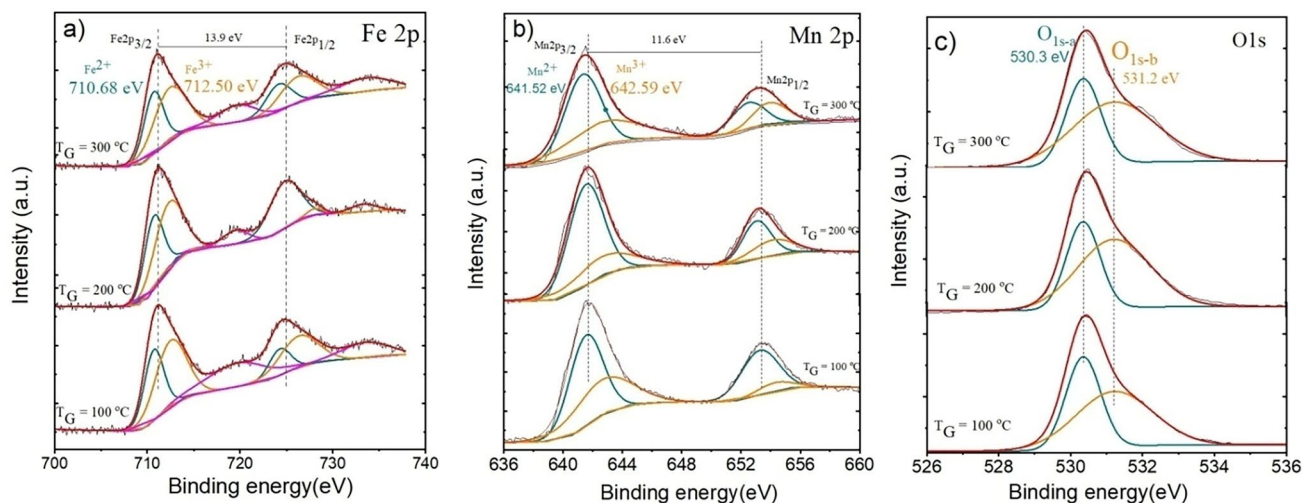


**Fig. 4** (Color online) **a** XPS spectra of Fe2p, **b** Mn2p and **c** O1s of  $\text{FeMn}_2\text{O}_{4.6}$  films

there are co-existences of  $\text{Fe}^{2+}$ ,  $\text{Fe}^{3+}$ ,  $\text{Mn}^{2+}$  and  $\text{Mn}^{3+}$  valance in  $\text{FeMn}_2\text{O}_{4.6}$  films and the atomic ratio Fe: Mn of 1: 2.

The optical band gaps of  $\text{FeMn}_2\text{O}_{4.6}$  films are determined via absorption coefficient by ellipsometry spectroscopy in the range between 200 and 800 nm. By using the formula  $\alpha(h\nu) = \frac{4\pi k}{\lambda}$ , the optical bandgap is determined by:  $\alpha(h\nu) = A \left( (h\nu - E_g) \right)^n$ . The A is a constant,  $E_g$  is optical band gap,  $n = 2$  for direct band gap and  $n = 1/2$  for indirect band gap. The  $E_g$  is deduced in terms of relation between  $(\alpha h\nu)^2$  and  $h\nu$  at  $(\alpha h\nu)^2 = 0$  [28]. As shown in Fig. 5, the band gaps ( $E_g$ ) of films are estimated to be 3.44, 3.50 and 3.20 eV corresponding to 100, 200, and 300 °C of growth temperature. These optical band gaps has potential application as photocatalyst material under ultraviolet light [28–30]. As compare to other low conductive spinel ferrites, such as  $\text{NiFe}_2\text{O}_4$  (direct band gap of 2.35 and 2.8 eV)  $\text{CoFe}_2\text{O}_4$  (direct band gap of 1.44 eV) or  $\text{MnFe}_2\text{O}_4$  (direct band gap of 1.97 eV) [31–33], the above optical band gap are higher, especially the film are not conductive at room temperature which are expecting for application in spin-filter devices. The mechanism of conduction in spinel oxides is explained by hopping of electrons between the cations at octahedral site [9]. Manganese spinel compounds relate to high electrical conductivities because manganese has multiple valance states such as  $\text{Mn}^{2+}$ ,  $\text{Mn}^{3+}$ ,  $\text{Mn}^{4+}$  [34]. While  $\text{Mn}^{2+}$  is dominant at tetrahedral site and other valance states at octahedral site [11–15]. So, the conductive  $\text{FeMn}_2\text{O}_{4.6}$  films can be affected by mixed manganese valance states.

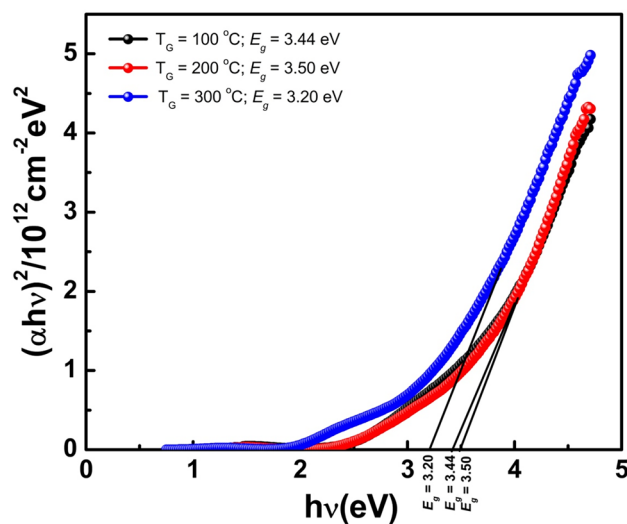
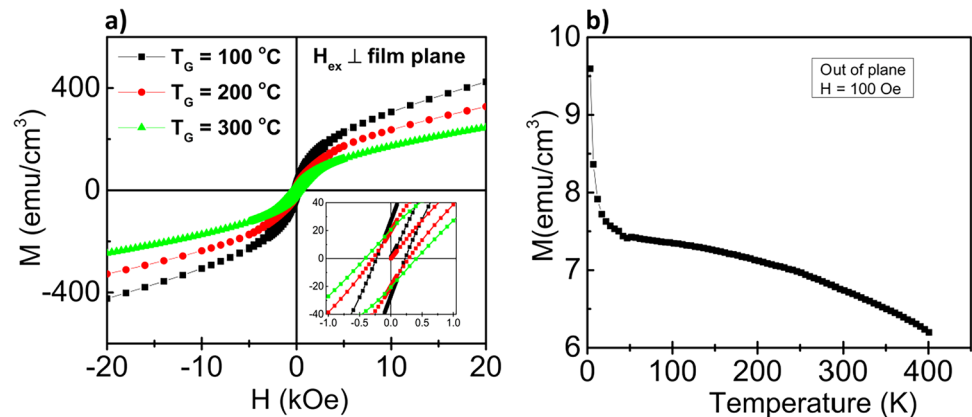


**Fig. 5** (Color online) Optical band gap of  $\text{FeMn}_2\text{O}_{4.6}$  films at growth temperatures 100 °C, 200 °C and 300 °C

Figure 6a shows the out-of-plane magnetization hysteresis (M–H) loops of  $\text{FeMn}_2\text{O}_{4.6}$  films at room temperature. The magnetization curves are not saturated under external magnetic field of 20 kOe, the value magnetization decreases as growth temperature increases, while coercivity ( $H_c$ ) has an opposite trend as indicated by insert Fig. 6a. The ferrimagnetism state in  $(\text{A}_{1-x}\text{B}_x)[\text{B}_{2-x}\text{A}_x]\text{O}_4$  spinel oxide originates from the interaction between magnetic moment of cation in each T and O sites: A–B, B–A is ferromagnetism, while the interaction between total moment of T and O is antiferromagnetism. The magnetic moment of bulk

**Fig. 6** (Color online) **a** Out-of-plane magnetization hysteresis (M–H) loops at room temperature, insert is the enlarge (M–H) loops **b** temperature-dependent magnetization (M–T) data of zero-field cooling (ZFC) under an external magnetic field of 100 Oe of sample growth at 300 °C



FeMn<sub>2</sub>O<sub>4</sub> is expected to be 4  $\mu_B$ /f.u by calculating Neel's model [9] assuming there are only Fe<sup>2+</sup>–4 $\mu_B$ , and Mn<sup>3+</sup>–4 $\mu_B$  in structural crystalline. However, the effective magnetic moment value is determined  $\sim 1.44\mu_B$ /f.u [10]. The magnetic moment is 4.3 $\mu_B$  in T sites, and 3.1 $\mu_B$  in O sites [11] while the cation distribution can be express (Mn<sup>2+</sup><sub>0.9</sub>Fe<sup>3+</sup><sub>0.1</sub>)<sub>T</sub> [Fe<sup>3+</sup><sub>0.8</sub>Fe<sup>2+</sup><sub>0.1</sub>Mn<sup>3+</sup><sub>1.1</sub>]<sub>O</sub>O<sub>4</sub>. The average magnetic moment per unit from saturation magnetization of hysteresis loops can be express:  $\mu_B = (M \times M_s) / 5585$  [35] here M is the molecular weight of the sample and M<sub>s</sub> is the saturation magnetization (emu/g), and 5585 is magnetic factor. However in this case the magnetic signal of FeMn<sub>2</sub>O<sub>4</sub> film was not saturated so estimating the magnetic moment of sample can be approximate. The results average magnetic moment per unit are estimated to be 3.72, 2.84, and 2.13  $\mu_B$ /f.u corresponding to 100, 200, and 300 °C of growth temperature. These value are smaller than the theory but larger than the experiment values [9, 10]. Thus, it can be inferred that the cation distribution in FeMn<sub>2</sub>O<sub>4-6</sub> films are mixed spinel. This result is consistent with the above Raman and XPS results. In the limitation of measurement results, the various magnetization and coercivity can be explained: (i) appearing strain between film and substrate, which modifies the magnetic properties of film compared to bulk material [36, 37]; (ii) the distributions of Fe<sup>2+</sup>, Fe<sup>3+</sup>, Mn<sup>2+</sup>, Mn<sup>3+</sup> at T and O sites change with growth temperature [38]. Tran et al. explained that the significant increase in H<sub>c</sub> and reduction in magnetization with growth temperature of epitaxial Fe film on BaTiO<sub>3</sub> (BTO) originated from the strain between film and substrate [36]. On the other hand Rajagiri et al. reported spontaneous magnetization increase with increasing growth temperature of MnFe<sub>2</sub>O<sub>4</sub> thin films due to change in valence state and cation distribution [38]. The variation of Fe<sup>3+</sup>/

Mn<sup>2+</sup> ratio at different growth temperature are almost similar in the above Raman and XPS results, the appearing strain between film and substrate, which modifies the magnetic properties of film can be main cause lead to the various magnetization and coercivity in FeMn<sub>2</sub>O<sub>4-6</sub> films. In Fig. 6b shows temperature-dependent magnetization (M–T) under zero-field cooling (ZFC) and an external magnetic field of 100 Oe of sample growth at 300 °C. Clearly, the curve exhibits ferrimagnetism state without any magnetic transition below room temperature. These results can be explained by reduction of tensile strain of FeMn<sub>2</sub>O<sub>4-6</sub> films as growth temperature increases [36, 37]. In addition, the effect of strain can be modified in terms of magnetic properties of FeMn<sub>2</sub>O<sub>4-6</sub> films compared to bulk material with and two magnetic transitions at 373 and 50 K [10].

## 4 Conclusion

In summary, FeMn<sub>2</sub>O<sub>4-6</sub> epitaxial films on MgO(001) substrates were successfully grown at various temperatures by using MBE. A tensile strain perpendicular to the surface is observed in FeMn<sub>2</sub>O<sub>4-6</sub> films with the decreasing value as increasing growth temperature. The effect of strain can be leads to the change of magnetic properties, and the magnetization value decreases as tensile strain decreases while coercivity increases. The films are not conductive at room temperature with optical band gaps of 3.44, 3.50, and 3.20 eV for growth temperature of 100 °C, 200 °C and 300 °C, respectively. Finally, the FeMn<sub>2</sub>O<sub>4-6</sub> films clearly show ferrimagnetic ordering at room temperature. The obtained results provide the structural, magnetic and optical of FeMn<sub>2</sub>O<sub>4-6</sub> thin films, which will

be useful for the research and fabrication of spin-filter devices.

## Acknowledgements

The authors would like to acknowledge the financial support of Hanoi University of Industry under the Grant number of 01 – 2024 – RD/HĐ-ĐHCNHN.

## Author contributions

DVT: Conceptualization, methodology, investigation, wrote and edited of the manuscript. NXC corrected the manuscript. NTT, NQT, HTH, DNT experiment, measurement and revised the manuscript. SLC approved the final version of the manuscript.

## Funding

This study was funded by Hanoi University of Industry under the Grant number of 01 – 2024 – RD/HĐ-ĐHCNHN.

## Data availability

All data available.

## Declarations

**Conflict of interest** All authors declare that they have no conflict of interest.

## References

1. R. Nepal, M. Saghayezhian, J. Zhang, R. Jin, J. Magn. Mater. **497**, 165955 (2020)
2. D. Srikala, S.D. Kaushik, M. Verma, Phys. Solid State **66**, 327–340 (2024)
3. J. Moussy, J. Phys. D Appl. Phys. **46**, 143001 (2013)
4. T.S. Santos, J.S. Moodera, Phys. Rev. B **69**, 241203 (2004)
5. M. Gajek, M. Bibes, A. Barthélémy, K. Bouzehouane, S. Fusil, M. Varela, J. Fontcuberta, A. Fert, Phys. Rev. B **72**, 020406 (2005)
6. C. Qi, Q. Liu, Y. Dong, G. Zhang, X. Jiang, D. Gao, RSC Adv. **12**, 27206–27211 (2022)
7. S. Nagamuthu, S. Vijayakumar, S.H. Lee, K.S. Ryu, Appl. Surf. Sci. **390**, 202–208 (2016)
8. V.S. Zhandun, A.V. Nemtsev, Mater. Chem. Phys. **259**, 124065 (2021)
9. D.S. Carballal, A. Roldan, R.G. Crespo, N.H. de Leeuw, Phys. Rev. B **91**, 195106 (2015)
10. R. Nepal, Q. Zhang, S. Dai, W. Tian, S.E. Nagler, R. Jin, Phys. Rev. B **97**, 024410 (2018)
11. B. Boucher, R. Buhl, M. Perrin, J. Appl. Phys. **40**, 1126 (1969)
12. M. Tanaka, T. Mizoguchi, Y. Aiyama, J. Phys. Soc. Jpn. **18**, 1091–1091 (1963)
13. A.P.B. Sinha, N.R. Sanjana, A.B. Biswas, Acta Cryst. **10**, 439 (1957)
14. Q. Zhang, W. Tian, R. Nepal, A. Huq, S. Nagler, J.F. DiTusa, R. Jin, Chem. Mater. **35**, 2330–2341 (2023)
15. A.A. Spivakov, C.R. Lin, E.S. Lin, Y.Z. Cheng, Y.T. Tseng, Nanoscale Res. Lett. **16**, 162 (2021)
16. L. Malavasi, P. Galinetto, M.C. Mozzati, C.B. Arroni, F. Flor, Phys. Chem. Chem. Phys. **4**, 3876 (2002)
17. Q. Tian, Q. Wang, Q. Xie, J. Li, Nanoscale Res. Lett. **5**, 1518 (2010)
18. Z. Wang, P. Lazor, S.K. Saxena, H.S.C. O’Neil, Mater. Res. Bull. **37**, 1589–1602 (2002)
19. J.L. Ortiz-Quiñonez, U. Pal, M.S. Villanueva, ACS Omega **3**(11), 14986–15001 (2018)
20. K.J. Kim, J. Park, J. Sol-Gel Sci. Technol. **92**, 40–44 (2019)
21. M. Baghaie Yazdi, K.-Y. Choi, D. Wulferding, P. Lemmens, L. Alff, New J. Phys. **15**, 103032 (2013)
22. R. Pazik, E. Piasecka, M. Małecka, V.G. Kessler, B. Idzikowski, Z. Śniadecki, R.J. Wiglusz, RSC Adv. **3**, 12230 (2013)
23. S. Thota, S.C. Kashyap, S.K. Sharma, V.R. Reddy, J. Phys. Chem. Solids **91**, 136 (2016)
24. H. Li, B. Song, W.J. Wanga, X.L. Chen, Mater. Chem. Phys. **130**, 39 (2011)
25. D. Varshneya, A. Yogi, Mater. Chem. Phys. **128**, 489 (2011)
26. K.J. Kim, H.J. Lee, J.Y. Park, J. Magn. Mater. **321**, 3706 (2009)
27. T. Fujii, F.M.F. de Groot, G.A. Sawatzky, F.C. Voogt, T. Hibma, K. Okada, Phys. Rev. B **59**, 3195 (1999)
28. S. Zinatloo-Ajabshir, M. Salavati-Niasari, J. Mol. Liq. **216**, 545–551 (2016)
29. S. Moshtaghi, S. Zinatloo-Ajabshir, M. Salavati-Niasari, J. Mater. Sci. Mater. Electron. **27**, 425–435 (2016)

30. S. Zinatloo-Ajabshir, S. Mortazavi-Derazkola, M. Salavati-Niasari, *J. Mater. Sci. Mater. Electron.* **28**, 17849–17859 (2017)
31. A.V. Ravindra, P. Padhan, W. Prellier, *Appl. Phys. Lett.* **101**, 161902 (2012)
32. M. Meinert, G. Reiss, *J. Phys. Condens. Matter* **26**, 115503 (2014)
33. M.Y. Rafique, P.L. Qing, Q. Javed, M.Z. Iqbal, Q.H. Mei, M.H. Farooq, G.Z. Gang, M. Tanveer, *Chin. Phys. B* **22**, 107101 (2013)
34. A. Petric, H. Ling, *J. Am. Ceram. Soc.* **90**(5), 1515–1520 (2007)
35. S. Singhal, K. Chanda, *J. Solid State Chem.* **180**, 296 (2007)
36. T.T. Tran, V. Nguyen, S. Cho, *J. Magn. Mater. Magn. Mater.* **578**, 170705 (2023)
37. Y. Hwang, J. Choi, S. Hong, S. Cho, S. Han, K. Shin, M. Jung, *Phys. Rev. B* **79**, 045309 (2009)
38. P. Rajagiri, B.N. Sahu, N. Venkataramani, S. Prasad, R. Krishnan, *AIP Adv.* **8**, 056112 (2018)

**Publisher's Note** Springer Nature remains neutral with regard to jurisdictional claims in published maps and institutional affiliations.

Springer Nature or its licensor (e.g. a society or other partner) holds exclusive rights to this article under a publishing agreement with the author(s) or other rightsholder(s); author self-archiving of the accepted manuscript version of this article is solely governed by the terms of such publishing agreement and applicable law.